

Cite this: *Dalton Trans.*, 2017, **46**, 8204

Theoretical and experimental studies on three water-stable, isostructural, paddlewheel based semiconducting metal–organic frameworks†

Xiaowei Yang,^{‡a} Yuan Zhang,^{‡b} Feng Li,^a Tiantian Guo,^a Yong Wu,^a Fengyan Jin,^a Min Fang,^{‡a,c,d} Yaqian Lan,^{‡a} Yafei Li,^{*a} Yong Zhou,^{‡b} and Zhigang Zou^b

Three water-stable isostructural metal–organic frameworks (MOFs) of the general formula $[M_2(\text{TCS})(\text{BPY})]$ ($M = \text{Co}(\mathbf{1}), \text{Ni}(\mathbf{2})$ and $\text{Cu}(\mathbf{3})$; $\text{H}_4\text{TCS} = \text{tetrakis}(4\text{-carboxyphenyl}) \text{ silane}$, $\text{BPY} = 4,4'\text{-bipyridine}$) were synthesized and fully characterized. MOFs **1–3** are stable in pH = 5–11, 2–11, 3–11 aqueous solution respectively for at least 24 h at room temperature. Although H_4TCS absorbs only UV light, MOFs **1–3** absorb both UV and visible light in broad ranges (250–800 nm) and absorb more visible light than the ligand BPY. The rapid anodic photocurrent responses of MOFs **1–3** under UV and visible light illumination were observed. The photocurrent densities increase in the order of MOF **3** < **1** < **2** under visible light illumination (430 nm). The band gaps of MOFs **1–3** determined based on UV-Vis diffuse reflectance spectra and electrochemical (EC) analysis are 1.28, 1.35 and 0.67 eV, respectively. MOF **1** is able to photocatalyze the reduction of CO_2 to CH_4 under visible light, producing CH_4 ($1.44 \mu\text{mol g}^{-1}$ in 8 h), which is unprecedented in MOFs. The catalytic activity of MOF **1** ($0.75 \mu\text{mol g}^{-1}$ after 4 h) under the irradiation of a 300 W xenon lamp is significantly better than those of MOFs **2** and **3** ($0.14 \mu\text{mol g}^{-1}$ after 4 h). The band structures, density of states and band gaps of MOFs **1–3** were calculated by the GGA-PBE and GGA-PBE+U method implemented in VASP code. The calculations show that all the three compounds can be viewed as bulk intermediate band (IB) materials. The density of states of the IB in MOF **1** is high, which could suppress the non-radiative recombination. The density of states of the IB levels in MOFs **2** and **3** are low, making these levels very effective recombination centres, thus jeopardizing the photocatalytic activities of MOFs **2** and **3**. The calculated results are in good agreement with experimental results and explain the photocatalytic activity differences. This study is the first to successfully address the question of how the types of unpaired electron containing electron-rich metal ions (*i.e.* $\text{Cu}(\text{II})$, $\text{Co}(\text{II})$, $\text{Ni}(\text{II})$) affect the band gaps and band structures of MOFs and thus their photoelectronic properties.

Received 28th April 2017,
Accepted 1st June 2017

DOI: 10.1039/c7dt01560g

rsc.li/dalton

^aDepartment of Chemistry, School of Chemistry and Materials Science, Nanjing Normal University, Nanjing 210023, China. E-mail: fangmin@njnu.edu.cn, liyafei@njnu.edu.cn

^bEcomaterials and Renewable Energy Research Center (ERERC), Nanjing University, 22 Hankou Road, Nanjing, Jiangsu 210093, P. R. China. E-mail: zhouyong1999@nju.edu.cn

^cState Key Laboratory of Coordination Chemistry, Nanjing University, Nanjing 210093, China

^dJiangsu Key Laboratory for Numerical Simulation of Large Scale Complex Systems (NSLSCS), Nanjing Normal University, Nanjing 210023, China

† Electronic supplementary information (ESI) available. CCDC 1440032 (MOF **1**), 1445198 (MOF **2**) and 1056672 (MOF **3**). For ESI and crystallographic data in CIF or other electronic format see DOI: 10.1039/c7dt01560g

‡ These authors contributed equally to this work.

Introduction

Solar energy is an inexhaustible and clean energy source worldwide. Semiconductors can convert sunlight into electricity or be photocatalysts utilizing sunlight in important chemical processes, for example in water splitting to hydrogen and oxygen, in CO_2 reductions which convert the greenhouse gas to fuels (such as CH_4 , CH_3OH , CO , C_2H_6 and so on) or in making other valuable chemicals.^{1,2} Most of the reported photocatalysts are active only in the ultraviolet (UV) region. Given that UV light accounts for only 4% while visible light contributes 43% of solar energy, it is rather imperative to develop visible-light-responsive photocatalysts.³ Metal–organic frameworks (MOFs), also called coordination polymers (CPs) are compounds consisting of metal ions or clusters coordinated to organic ligands to form two-, or three-dimensional structures.

These materials can be synthesized as narrow-band semiconductors due to their designability.^{4,5} Studies relating to the semiconducting behaviours of MOFs are still in their initial stages, and further investigations are highly desired.⁵ There have been only a few reports on the optoelectronic properties of semiconducting MOFs.^{6–13} The photocatalytic reduction of CO₂ to CH₄ in the presence of H₂O involves the transfer of 8 electrons (eqn (1)), making CH₄ harder to observe than other CO₂ reduction products such as HCOOH. Few studies were published on the CO₂ reduction to CH₄ using MOFs as photocatalysts,^{14,15} and no results under only visible light were reported.

How to decrease the band gaps of MOFs to make visible light absorbing semiconductors has become an important issue. Based on experimental and theoretical results, Lu *et al.*⁵ concluded that the band gap of semiconducting MOFs can be decreased by: (i) increasing the conjugation in the linker, (ii) selecting electron-rich metal nodes and organic molecules, and (iii) functionalizing the linker with nitro and amino groups. However, few examples of using electron rich metal ions to make narrow-band MOFs were reported.⁵ In addition, the question of how the types of unpaired electron containing electron-rich metal ions (*i.e.* Cu(II), Co(II), Ni(II)) affect the band gaps and band structures of MOFs is yet to be answered. DFT calculations on these metal ion-based MOFs are expensive and few reports have been published.¹⁶

On the other hand, relatively low water and thermal stabilities of most MOFs could be the key limitations for their practical applications.¹⁷ Our group aims to synthesize and characterize water-stable MOFs.^{18–20} Generally, MOFs containing tri- or tetravalent metal cations, such as Cr³⁺, Al³⁺, Fe³⁺, Ti⁴⁺ or Zr⁴⁺ and ZIFs (zeolitic imidazolate frameworks) display a high degree of stability toward water.^{18,21–31} Generally, MOFs based on paddlewheel structures of divalent metal ions are found unstable towards water.^{32–35} Nonetheless, we have recently reported a water-stable, paddlewheel based Zn(II) MOF, [Zn₂TCS(BPY)] (H₄TCS = tetrakis(4-carboxyphenyl) silane, BPY = 4,4'-bipyridine) (**4**).¹⁹

H₄TCS is an easily-prepared,³⁶ rigid and large tetrahedral ligand, which favours the formation of large pore MOFs. Many MOFs based on this ligand have been reported.^{19,20,37–50} It is worth noting that H₄TCS only absorbs UV light. Herein through applying electron-rich metal ions and the electron rich ligand BPY, we obtained three visible-light absorbing, water-stable isostructural, two-fold interpenetrated paddlewheel MOFs of the general formula [M₂(TCS)(BPY)] [M = Co(1) and Ni(2) and Cu(3)]. MOFs 1–3 absorb both UV and visible light in broad ranges (250–800 nm), and absorb more visible light than the ligand BPY. The three MOFs exhibit semiconducting behaviours, with the photocurrent density increasing in the order of MOF 3 < 1 < 2 upon visible light (430 nm) illumination, being consistent with their experimental band gaps of 1.35, 1.28 and 0.67 eV for MOFs 2, 1 and 3, respectively. Moreover, they are found to catalyze the reduction of CO₂ to CH₄ under visible light irradiation in the presence of H₂O vapour, which is rarely reported amongst MOFs. The band

structures, orbital populations and band gaps of MOFs 1–3 were calculated by the GGA-PBE and GGA-PBE+U method implemented in VASP code. The calculated results are in good agreement with the experimental results, and account for photocatalytic properties and activity differences of MOFs 1–3.

Experimental

Materials and general methods

H₄TCS was prepared by a procedure previously reported in the literature,³⁶ other chemicals and reagents were obtained from commercial sources and used without further purification. Elemental analyses for C, H and N were performed on a Vario EL III elemental analyzer. Infrared spectra (FTIR) were recorded in the range 4000–400 cm⁻¹ on a NEXUS670 (resolution: 0.01 cm⁻¹) gas chromatography-infrared spectrometer. The Raman spectra were recorded on a Jobin Yvon LabRam HR800 Confocal Micro-Raman Spectrometer using an Ar 514.5 nm laser line, with a resolution of 3 cm⁻¹. TG analyses were carried out using the SDT 2980 thermal analyzer under an air flow of 15 mL min⁻¹ over a temperature range from 25 to 800 °C at a heating rate of 5 °C min⁻¹. Powder X-ray diffraction (PXRD) patterns were recorded on a Bruker D8 Advance instrument using Cu K α radiation ($\lambda = 1.54056 \text{ \AA}$) with a scan speed of 0.1 s per degree at room temperature. The solid-state UV/Vis diffuse reflectance spectra were recorded with a Varian Cary 5000 UV-Vis-NIR in the range $\lambda = 200\text{--}800 \text{ nm}$. Gas adsorption/desorption measurements were performed with a Quantachrome Instruments Autosorb AS-6B extended pressure adsorption analyzer. The as-synthesized samples were activated for 10–12 h at 150 °C under vacuum prior to gas adsorption-desorption measurements.

Chemical stability tests. About 20 mg of an as-synthesized sample was soaked in different pH aqueous solutions (obtained by adding a suitable amount of HCl or NaOH aqueous solution) at room temperature for 24 h. The sample was then filtered and heated at 60 °C for 12 h. PXRD measurements were performed to check the structural stability.

Syntheses

Synthesis of MOF 1, Co₂(TCS)(BPY) in H₂O. H₄TCS (12.8 mg, 0.025 mmol), BPY (7.8 mg, 0.05 mmol) and CoCl₂·6H₂O (23.8 mg, 0.100 mmol) in 9.0 mL H₂O were stirred for 30 min in a glass vial. The glass vial was then placed in an autoclave equipped with a Teflon liner (25 mL) and put into an oven. The temperature of the oven was then raised to 150 °C at a rate of 1 °C min⁻¹, kept at 150 °C for 3 d, and was cooled down to room temperature at a rate of 0.2 °C min⁻¹. Large dark-blue, block-like crystals were obtained with small amounts of colourless needle crystals. The colourless needle crystals were broken into small pieces by ultrasonication and then were decanted, leaving block-like crystals of **1**. The crystals were washed with water, filtered and dried at 40 °C for 6–7 h (yield: 17.8 mg, 89% based on H₄TCS). Its purity was checked by PXRD (Fig. S6(a) in the ESI†). FT-IR and Raman spectra are given in

Fig. 3(a) and (b) and tentative assignments are given in Table S1.† Elemental analysis of $[\text{Co}_2(\text{TCS})(\text{BPY})]\cdot\text{H}_2\text{O}$, calcd (%): C 56.3, H 3.2, N, 3.4; found (%): C 56.0, H 3.2, N, 3.5.

Synthesis of MOF 2, $\text{Ni}_2(\text{TCS})(\text{BPY})$ in H_2O . H_4TCS (6.4 mg, 0.0125 mmol), BPY (3.9 mg, 0.025 mmol), $\text{Ni}(\text{NO}_3)_2\cdot 6\text{H}_2\text{O}$ (14.6 mg, 0.050 mmol) and 50 μL HCl aqueous solution (2.0 mol L^{-1}) in 4.0 mL H_2O were stirred for 30 min in a glass vial. The glass vial was then placed in an autoclave equipped with a Teflon liner (25 mL) and put into an oven. The temperature of the oven was then raised to 170 $^\circ\text{C}$ at a rate of 1 $^\circ\text{C min}^{-1}$, kept at 170 $^\circ\text{C}$ for 2 d, and was cooled down to room temperature at a rate of 0.2 $^\circ\text{C min}^{-1}$. Green, block-like crystals were obtained with small amounts of colourless needle crystals. The colourless needle crystals were removed and the green crystals (washed with H_2O) of MOF 2 were recovered as described for MOF 1 (yield: 7.8 mg, 78% based on H_4TCS). Its purity was checked by PXRD (Fig. S6(b)†). FT-IR and Raman spectra are given in Fig. 3(c) and (d) and tentative assignments are given in Table S1.† Elemental analysis of $[\text{Ni}_2(\text{TCS})(\text{BPY})]\cdot\text{H}_2\text{O}$, calcd (%): C 56.3, H 3.2, N, 3.4; found (%): C 55.9, H 2.9, N, 3.6.

Synthesis of MOF 3, $\text{Cu}_2(\text{TCS})(\text{BPY})$ in water. The procedure is identical to the synthesis of MOF 2 in water except that $\text{Ni}(\text{NO}_3)_2\cdot 6\text{H}_2\text{O}$ was replaced by $\text{Cu}(\text{NO}_3)_2\cdot 6\text{H}_2\text{O}$ (14.8 mg, 0.050 mmol) and 100 μL instead of 50 μL HCl aqueous solution (2.0 mol L^{-1}) was added. Blue crystals of MOF 3 were recovered (yield: 8.8 mg, 87% based on H_4TCS). Its purity was checked by PXRD (Fig. S6(c)†). FT-IR and Raman spectra are given in Fig. 3(e) and (f) and tentative assignments are given in Table S1.† Elemental analysis of $[\text{Cu}_2(\text{TCS})(\text{BPY})]\cdot\text{H}_2\text{O}$, calcd (%): C 56.3, H 3.2, N, 3.4; found (%): C 56.0, H 3.2, N, 3.5.

Large scale synthesis of MOF 1 in DMF. H_4TCS (64 mg, 0.125 mmol), BPY (19.5 mg, 0.125 mmol) and $\text{Co}(\text{NO}_3)_2\cdot 6\text{H}_2\text{O}$ (145.5 mg, 0.50 mmol) in 20 mL DMF (dimethylformamide) were stirred for 10 min in a glass vial and then placed in an autoclave equipped with a Teflon liner (50 mL) and put into an oven. The temperature of the oven was then raised to 150 $^\circ\text{C}$ from room temperature, kept at 150 $^\circ\text{C}$ for 3 d, the heat was turned off, and the autoclave was cooled down to room temperature naturally in the oven, resulting in dark-blue powder. The powder was filtered and washed with DMF and then H_2O , dried at 60 $^\circ\text{C}$ for 12 h (yield: 80 mg, 80% based on H_4TCS). Its purity was checked by PXRD (Fig. S5(a)†).

Large scale synthesis of MOF 2 in H_2O . H_4TCS (51.2 mg, 0.100 mmol), BPY (16.0 mg, 0.100 mmol) and $\text{Ni}(\text{NO}_3)_2\cdot 6\text{H}_2\text{O}$ (116.3 mg, 0.40 mmol) in 32 mL H_2O were stirred for 10 min in a glass vial and then placed in an autoclave equipped with a Teflon liner (50 mL) and put into an oven. The temperature of the oven was then raised to 170 $^\circ\text{C}$ from room temperature, kept at 170 $^\circ\text{C}$ for 3 d, the heat was turned off, and the autoclave was then cooled down to room temperature naturally in the oven, resulting in dark-green block crystals. The crystals were washed with H_2O , dried at 60 $^\circ\text{C}$ for 12 h (yield: 55 mg, 69% based on H_4TCS). Its purity was checked by PXRD (Fig. S5(b)†).

Large scale synthesis of MOF 3 in H_2O . 96.8 mg $\text{Cu}(\text{NO}_3)_2\cdot 6\text{H}_2\text{O}$ (0.40 mmol) was added, and other synthetic procedures are the same as those of the large scale synthesis of MOF 2. Blue powder (yield: 50 mg, 62% based on H_4TCS) was obtained and its purity was checked by PXRD (Fig. S5(c)†).

X-ray crystallography

All MOFs with appropriate dimensions were chosen under an optical microscope, transferred into a glass fibre, and mounted onto a loop for single crystal X-ray data collection. Suitable crystals of three MOFs were selected for single crystal X-ray diffraction. The data were collected at 296 K on a Bruker Smart CCD diffractometer with graphite-monochromatic $\text{K}\alpha$ radiation ($\lambda = 0.71073 \text{ \AA}$) from an enhanced optic X-ray tube. Raw data for the structure were obtained using SAINT, and absorption correction was applied using SADABS programs. The structure was solved by direct methods and refined by full matrix least-squares on F^2 , using the SHELXS-2014 and SHELXL-2014 programs. Details of data collection, refinement parameters, and crystallographic data for the MOFs 1–3 and 5 (the non-interpenetrated counterpart of MOF 4) are summarized in Table S2.† The selected bond distances and angles of MOFs 1–3 are given in Table S3 of the ESI.† The crystallographic material can also be obtained from the CCDC, the deposition numbers are CCDC 1440032 (1) and 1445198 (2).†

Electrochemical (EC) analysis to determine conduction and valence band edges

MOF 1 (1.75 mg) (or MOF 2 (1.56 mg) or MOF 3 (1.77 mg)) was put into 0.5 mL water and sonicated for 3–4 h under 100 W. Then 20 μL of the above mixture was dropped to the indium tin oxide (ITO) electrode, the geometrical area of which was 0.28 cm^2 . The electrode was then dried at room temperature in a desiccator over silica gel for 2–3 days before applying it in EC analyses. The EC measurements were performed with a CHI 660D electrochemical workstation (CH Instruments Inc, USA). All experiments were carried out at room temperature using a conventional three-electrode system with the ITO electrode (sheet resistance 20–25 Ω per square) as the working electrode, a platinum wire as the auxiliary electrode, and an Ag/AgCl (saturated KCl) electrode as the reference electrode. Two different electrolytes were used, a Tris-HCl-buffered saline (0.1 mol L^{-1} , pH 7.4) and a pH 5.01 H_2SO_4 aqueous solution. A linear potential scan (100 mV s^{-1}) was conducted to determine the conduction- and valence-band edges of MOFs 1–3.

The photoelectrochemical (PEC) measurements

The modified ITO electrodes were prepared as described above, except for the applied amounts of MOFs 1–3. In this case, MOF 1 (1.50 mg), 2 (1.54 mg) or 3 (1.46 mg) was put into 0.5 mL water and sonicated. The photoelectrochemical (PEC) measurements were performed with a Zahner PEC workstation (Zahner, Germany). All experiments were carried out at room temperature using a conventional three-electrode system with the above modified ITO electrode (sheet resistance 20–25 Ω

per square) as the working electrode, a platinum wire as the auxiliary electrode, and an Ag/AgCl electrode as the reference electrode. Every cycle was operated with the light-on time of 20 seconds and light-off time of 30 seconds and continued for 4–5 cycles. PEC measurements were carried out under 385 or 430 nm light irradiation at a constant potential (*versus* Ag/AgCl) in Tris-HCl buffered saline (0.1 mol L⁻¹, pH 7.4).

Measurement of the photocatalytic activity

MOFs 1–3 used in photocatalytic studies were synthesized by large scale synthetic methods. 0.10 g of the as-prepared sample was uniformly dispersed on the circular glass reactor with an area of 4.2 cm². A 300 W xenon arc lamp was used as the light source and a 420 nm cutoff filter was used to obtain visible light. The volume of the reaction system was about 230 ml. The reaction setup was evacuated at room temperature for 3–4 h, and then at ambient pressure, high purity CO₂ gas was introduced into the reaction setup. 0.4 mL of deionized water was injected into the reaction system as the reducing agent. The as-prepared photocatalyst was allowed to equilibrate under the CO₂/H₂O atmosphere for several hours to ensure that the adsorption of gas molecules was complete. During the irradiation, about 1 mL of gas was continually taken from the reaction cell at given time intervals for subsequent CH₄ concentration analysis by using a gas chromatograph (GC-2014, Shimadzu Corp., Japan).

Computational methodology

Density functional theory (DFT) computations were performed using the plane-wave technique implemented in the Vienna *ab initio* simulation package (VASP).⁵¹ The ion–electron interaction is described using the projector-augmented plane wave (PAW)⁵² approach. The generalized gradient approximation (GGA)^{53,54} expressed by the Perdew, Burke, and Ernzerhof (PBE)⁵⁵ functional and a 500 eV cutoff energy for the plane-wave basis set were adopted in all computations. The conjugated-gradient algorithm based on Hellmann–Feynman forces was used to relax the ions into their instantaneous equilibrium positions.

Because we deal with relatively large systems (150 atoms per unit cell), we used the *G*-point to sample the Brillouin zone using the Monkhorst–Pack scheme during geometry optimizations. Static electronic structure and DOS calculations were performed on the fully optimized structure with the *k*-point grid of 2 × 2 × 1 using the Monkhorst–Pack scheme. We set the convergence criteria for energy and force to be 0.1 × 10⁻⁴ eV and 0.02 eV, respectively, for all calculations. In all calculations, the precision parameter was set as medium. Brillouin-zone integration is performed with a Gaussian broadening of 0.2 eV.

Since Co²⁺, Cu²⁺ and Ni²⁺ contain partially filled d orbitals, compounds 1–3 could have open shell configurations and be strongly correlated electron materials (SCEMs). It was reported that the DFT method cannot describe SCEMs accurately.⁵⁶ We therefore used both the GGA-PBE method and GGA-PBE+U formalism as implemented in VASP following Dudarev's

method⁵⁷ to calculate the SCF, DOS and BS of compounds 1–3. This method divides the electrons into two classes: delocalized s and p electrons, which can be well-described by the GGA-PBE method, and the localized d electrons, which are described by Coulomb and exchange corrections. Different *U* values are applied besides the reported *U* values (3.3, 6.4, and 4.0 eV for Co, Ni, and Cu, respectively);⁵⁸ *U* = 4 and *J* = 1 for transition metal d orbitals.^{59,60}

Results and discussion

Syntheses

MOFs 1–3 can be synthesized in H₂O and other organic solvents. The reaction temperatures in H₂O need to be higher than those in organic solvents, probably due to the poor solubility of H₄TCS in water. Pure crystals and powder of MOF 1 were synthesized in H₂O and DMF, respectively. Pure MOF 2 was only obtained when using water as the solvent. Pure MOF 3 can be obtained in both water and the 1 : 1 volume ratio of DMA (dimethylacetamide) and DMF mixed solvent (Fig. S6†). Convenient and large scale syntheses of MOFs 1–3 were achieved, which is important for further investigations for their applications in various fields.

Structures

MOFs 1–3 are isostructural, and isostructural to our recently published two-fold interpenetrated Zn₂(TCS)(BPY) (4)¹⁹ based on PXRD (powder X-ray diffraction) evidence. The brief description of the crystal structure of MOF 3 and Zn₂(TCS)(BPY) (5) which is the non-interpenetrated counterpart of 4, are also given in ref. 19. The coordination environments of the ligand and metal ions of MOF 1 are given in Fig. 1. Every two metal ions and 4 carboxylate groups form a paddlewheel substructural building unit (SBU). Each paddlewheel unit also coordinates with two BPY ligands. Each TCS⁴⁻ ligand connects with 4 paddlewheel SBUs. Although connectivities are the same, MOFs 1 and 3 crystallize in the tetragonal *Pa*₂/*mmm* space group, while MOF 2 crystallizes in a lower symmetry, orthogonal space group (*Pccm*). Correspondingly, the asymmetric unit of MOF 2 is different from those of MOFs 1 and 3

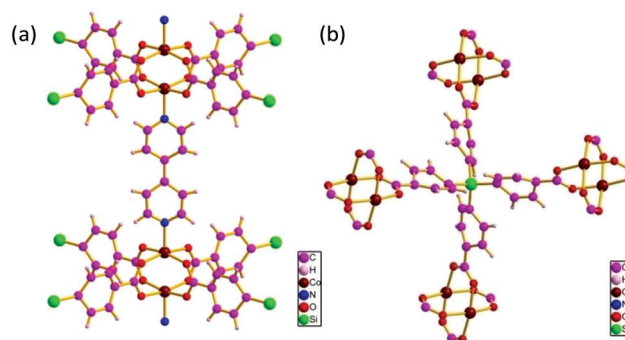


Fig. 1 The coordination environment of the metal ions and ligands of 1.

as shown in Fig. S7.† In contrast, the reported paddlewheel $[M_2(BTB)_{4/3}(BPY)]$ ($M = Co, Cu, Zn$)^{61,62} all crystallize in the same $Pm\bar{3}n$ space group. The phenyl ring and BPY ring carbon atoms are disordered in MOFs 1–3, which is most severe in MOF 2. Our efforts (growing single crystals of better quality and collecting diffraction data at 100 K) to alleviate the disorder of 2 were not successful.

The packings of MOFs 1 and 2 are given in Fig. 2 (the view along b and c directions are given in Fig. S8†). MOFs 1 and 2 have two-fold interpenetrated structures as illustrated in Fig. 2(c) and (d). They belong to the 3D binodal (4,6)-connected $sqc422$ net with a point symbol of $(4^2 \cdot 5^{10} \cdot 7^2 \cdot 8)(4^2 \cdot 5^4)$.¹⁹ The porosity and pore sizes of MOFs 1–3 are measured and given in Table S4.† The pore sizes of MOFs 1–3 are similar and are very small, not more than 3.6 Å. The porosities of MOFs 1–3 are very similar, not more than 17%.

IR and Raman spectra

Vibrational spectra are very useful to monitor the structural changes of MOFs in various processes. DeCoste *et al.*^{63,64} studied the water stability of $Cu_3(BTC)_2$ and Zr-MOFs by both PXRD and IR spectroscopy. Their results indicate that IR is slightly more sensitive to the structure changes than the PXRD patterns. The IR and Raman spectra of 1–4 (Fig. 3) are very similar to each other, and the tentative assignments of the vibrational frequencies are given in Table S1.† The details of the assignments are given in the ESI.†

Water and thermal stability

Thermogravimetric (TG) analysis was carried out to examine the thermal stability of MOFs 1–3 (Fig. 4). MOFs 1–3 undergo a weight loss of 2.1, 2.5 and 3.1% respectively before 100 °C, corresponding to the loss of free lattice water molecules within the pores or on the surface of the material. The decomposition

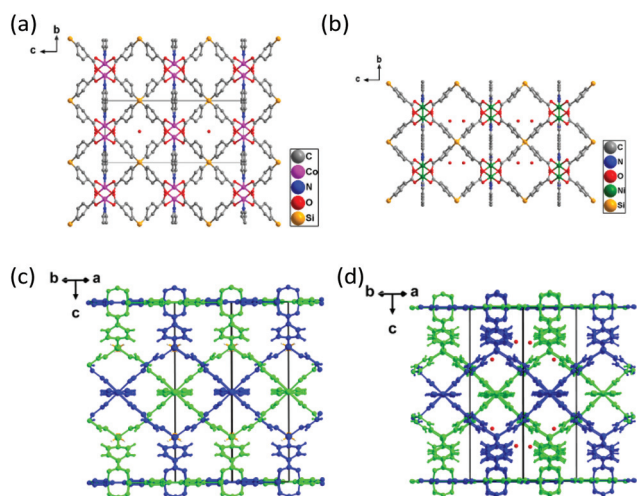


Fig. 2 The 3D packing of MOFs 1 and 2, viewing along the a ((a) (1) and (b) (2)), $a + b$ ((c) (1) and (d) (2)) axes. (c) and (d) show the two-fold interpenetration structures of MOFs 1 and 2, respectively.

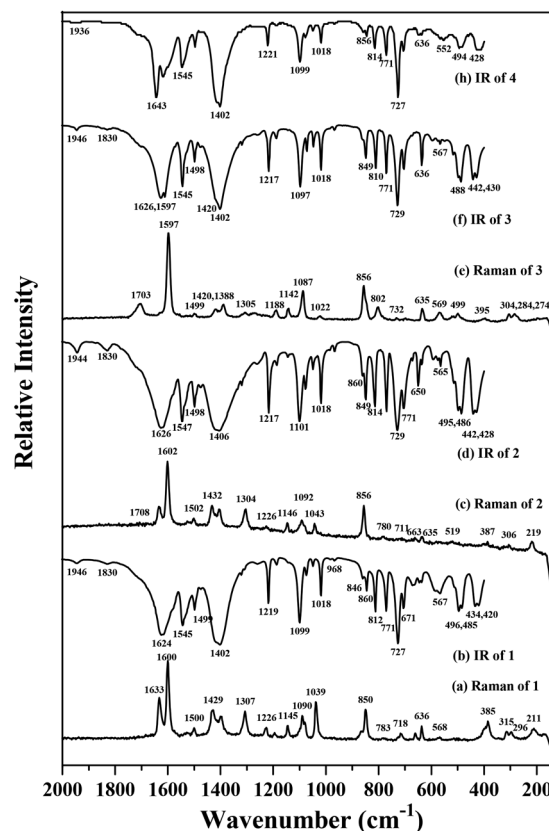


Fig. 3 FT-IR and Raman spectra of 1–3 and 4 (4000–400 cm^{-1} in Fig. S2 of the ESI,† IR of MOF 4 are from the ESI of ref. 19).

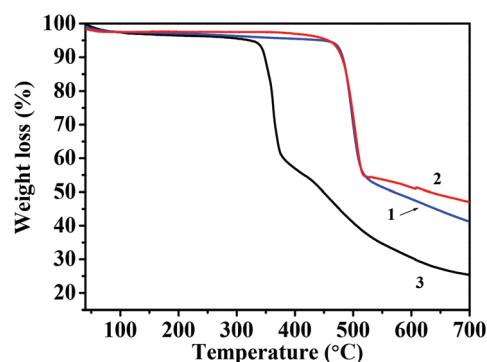


Fig. 4 Thermogravimetric analysis of the as-synthesized MOFs 1–3.

of the frameworks occurs at about 450 °C for MOFs 1 and 2, and 320 °C for MOF 3 according to the TG analysis.

The robustness and thermal stability of the framework of 1–3 were further checked by powder X-ray diffraction. During the gas adsorption measurements, we found that MOF 3 decomposes after heating at 150 °C for 10–12 h under vacuum several times, but MOF 2 remains intact under the same treatment. MOF 3 after heating at 200 °C for 12 h shows signs of decomposition in its IR spectrum (appearance of the band at 1703 cm^{-1} ($\nu(CO)$ of COOH as shown in Fig. S10 of the ESI†)

and decrease of the band at 1611 cm^{-1}), but not in its PXRD spectrum, indicating that IR is more sensitive than PXRD. PXRD (Fig. S9†) and IR spectra (Fig. S10†) indicate that MOFs 1 and 2 are stable after heating at 200 °C for 12 h and DMF in MOF 1 can be completely removed under these conditions. These studies indicate that the thermal stability of MOFs decrease in the order of $2 \approx 1 > 3$.

MOFs 1–3 are found to be stable in pH = 5–11, 2–11, 3–11 aqueous solution for at least 24 h indicated by PXRD patterns shown in Fig. 5. The PXRD pattern of MOF 2 shows changes after the MOF was put into pH = 11 aqueous solution for 24 h. We recovered the sample (washed with pure water) and heated the sample at 200 °C for 12 h, and the PXRD of the heated sample has the same pattern as those of the simulated based on structural information (Fig. S9(e)†) and its IR spectrum is also just like that of the as-synthesized sample (Fig. S10†), indicating that MOF 2 is stable in pH = 11 aqueous solution. After MOF 3 was put into pure water for 24 h, the sample was recovered and its CO_2 adsorption at 298 K remains the same (Table 1 and Fig. S13†), indicating that it is stable in water.

Adsorption properties

The as-synthesized samples were activated for 10–12 h at 150 °C under vacuum prior to any gas sorption measurement. N_2 gas sorption isotherms at 77 K of MOFs 1–3 (Fig. S11†) indicate that only surfaces of MOFs 1–3 adsorbed N_2 molecules. The N_2 uptake of MOFs 1–3 is 70 , 60 and $110\text{ cm}^3\text{ (STP) g}^{-1}$, respectively; and the Brunauer–Emmett–Teller (BET) specific surface area is 28 , 21 and $46\text{ m}^2\text{ g}^{-1}$, respectively.

The sorption isotherms for H_2 (at 77 K), CO_2 (298 and 273 K) and CH_4 (298 and 273 K) are shown in Fig. S12† and the adsorption capacities at 1 atm are given in Table 1. The adsorption capacities are good considering their small porosity (<17%).^{65–67} The adsorption capacity of H_2 at 77 K and 1 atm is MOF 4 (Zn(II)) > 2 (Ni(II)) > 3 (Cu(II)) > 1 (Co(II)). The adsorption capacities for CH_4 and CO_2 at 273 and 298 K increase in the order 4 (Zn(II)) > 1 (Co(II)) \approx 3 (Cu(II)) > 2 (Ni(II)). Dincă *et al.*⁶⁸ also reported that $\text{Cu}_3(\text{BTC})_2$ has higher CO_2 adsorption capacity than that of its isostructural MOF, $\text{Ni}_3(\text{BTC})_2$, consistent with our finding. As reported, the adsorption capacity of CO_2 (296 K, 1 atm) and H_2 (77 K, 1 atm) of MOF-74 (M = Zn(II), Co(II), Ni(II)) increases in the order of Co(II) > Ni(II) > Zn(II)⁶⁹ (consistent with our finding) and Ni(II) > Co(II) > Zn(II),⁷⁰ respectively.

UV-Vis diffuse reflectance spectra

UV-Vis diffuse reflectance spectra of MOFs 1–3 and ligands H_4TCS and BPY in the form of absorbance *versus* wavelength are shown in Fig. 6(a). The spectra in the form of $R\%$ (reflectance) *versus* wavelength are given in Fig. S14.† MOFs 1–3 absorb broadly in the visible light region. MOF 3 absorbs more visible light than MOF 1, which absorbs more visible light

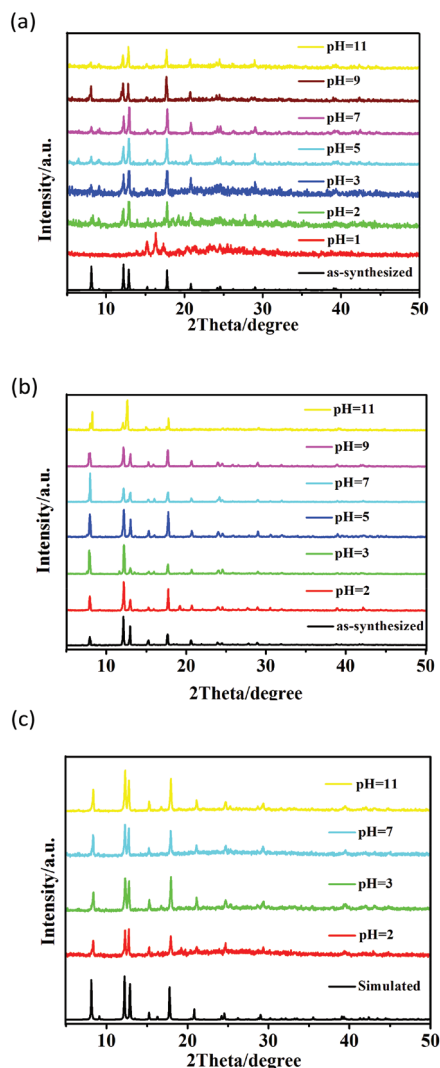


Fig. 5 Stability of 1 (a), 2 (b) and 3 (c) in water checked by PXRD.

Table 1 Adsorption capacities of MOFs 1–4

	N_2 77 K $\text{cm}^3\text{ g}^{-1}$ (%)	H_2 77 K $\text{cm}^3\text{ g}^{-1}$ (%)	CO_2 298 K $\text{cm}^3\text{ g}^{-1}$ (%)	CO_2 273 K $\text{cm}^3\text{ g}^{-1}$ (%)	CH_4 298 K $\text{cm}^3\text{ g}^{-1}$ (%)	CH_4 273 K $\text{cm}^3\text{ g}^{-1}$ (%)
1	70	91.9 (0.82)	36.9 (7.25)	56.7 (11.1)	5.7 (0.41)	13.7 (0.98)
2	60	104.2 (0.93)	28.0 (5.50)	42.8 (8.41)	3.7 (0.26)	10.1 (0.72)
3	110	97.2 (0.87)	34.2 (6.72) (35.8) (7.03) ^b	52.7 (10.4)	6.2 (0.44)	12.9 (0.92)
4 ^a	156	150 (1.34)	47 (9.2)	85 (16)	—	19 (1.4)

^a Data are from ref. 19. ^b The adsorption capacity of MOF 3 recovered after putting in water for 24 h.

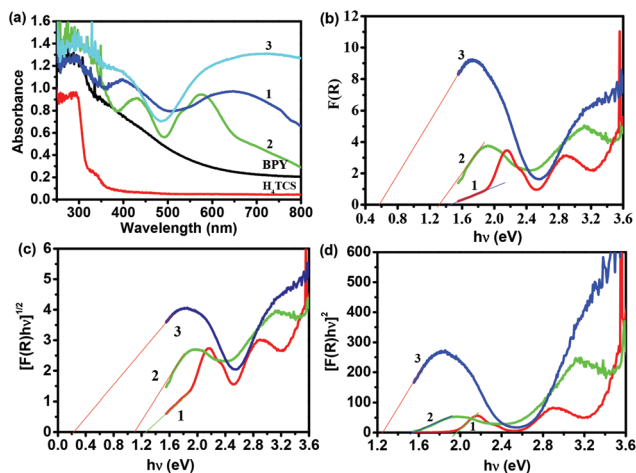


Fig. 6 (a) UV-Vis reflectance spectra of MOFs 1–3 in the form absorbance versus wavelength; (b)–(d) band gaps of MOFs 1–3 determined by plots of $F(R)$, or $(F(R)hv)^{1/2}$ or $(F(R)hv)^2$ versus hv .

than MOF 2; and they all adsorb more visible light than H_4TCS and BPY. The band gaps of MOFs 1–3 can be determined as the intersection point between the energy axis (hv) and the line extrapolated from the linear portion of the adsorption edge in the plots of the Kubelka–Munk function ($F(R)$) versus energy (hv) (Fig. 6(b)).^{71,72} $F(R)$ equals $(1 - R)^2/(2R)$ where R is the reflectance in the UV-Vis diffuse reflectance spectra. Alternatively, the band gaps of materials can be calculated by using the following equation:^{73–76}

$$\alpha hv = A(hv - E_g)^{n/2}$$

where α , ν , E_g , and A are the absorption coefficient, light frequency, band gap, and a constant, respectively. n is determined by the optical transition type of the semiconductor (*i.e.*, n equals 1 for direct allowed transition and 4 for indirect forbidden transition).⁷⁵ Because α is proportional to $F(R)$,^{75,76} the

energy intercept of a plot of $(F(R)hv)^2$ versus energy (hv) yields E_g for a direct allowed transition when the linear region is extrapolated to zero coordinate, and the energy intercept of a plot of $(F(R)hv)^{1/2}$ versus energy (hv) yields E_g for an indirect allowed transition (Fig. 6(c) and (d)). We calculated the band gaps in the above three ways and the results are given in Table 2. It is found that the E_g determined by the plots of $(F(R)hv)^{1/2}$ versus $hv < E_g$ determined by the plots of $F(R)$ versus $hv < E_g$ determined by the plots of $(F(R)hv)^2$ versus hv . When the semiconductor type of material is not clear, the results suggest it is better to use the plots of $F(R)$ versus hv to determine the E_g .

Determination of the conduction and valence band edges of MOFs 1–3 using the electrochemical (EC) method

This study subjected the conduction band edge (LUMO) and valence band edge (HOMO) positions of MOFs 1–3 to analyses with linear potential scans according to the method given in the literature.^{77,78} The band edge positions vs. Ag/AgCl electrodes and the normal hydrogen electrode (NHE) are given in Table 2. The detailed method of obtaining these results is given in the ESI.† Band gaps and band edges determined with the EC methods for MOFs 1 and 3 (see below) are consistent with the band gaps determined by the plots of $(F(R)hv)^{1/2}$ versus hv , much less with the results by the plots of $(F(R)hv)^2$ versus hv suggesting that MOFs 1 and 3 are indirect band-gap semiconductors. The experimental results cannot explain the semiconductor type of MOF 2, and are most consistent with the results obtained by the plot of $F(R)$ versus energy (hv). Consistently, the calculated band structure of MOF 2 shows that the top of the VB and the bottom of the CB of MOF 2 are very flat. Thus, by using the EC method and UV-Vis reflectance spectra, we are able to obtain the band gaps, the valence and conduction band edge positions, and some information about the semiconductor types of materials. The determined values are presented in Table 2.

Table 2 Theoretically and experimentally determined band gaps (E_g in eV) and band positions (eV)

MOF	Calcd band positions ^a	Calcd E_g	Exp. E_g by plots of $F(R)$ vs. $hv^{b,c}$	Exp. E_g by plots of $(F(R)hv)^{1/2}$ vs. $hv^{b,c}$	Exp. E_g by plots of $(F(R)hv)^2$ vs. $hv^{b,c}$	Exp. E_g and the HOMO and LUMO band positions vs. Ag/AgCl electrode ^c	Exp. band positions vs. NHE electrode
1	GGA-PBE: 1.74–2.18, 0.58–1.13, –0.70, –0.96, –1.25, –1.52, –1.66, $U = 4.0, J = 1.0$: 0.86, –0.87	1.29, 1.74	1.45	1.23	1.96	1.28 (–0.23, 1.05)	–0.03, 1.25
2	$U = 3.3$: spin up: 2.14–2.61, 1.63, 0.30, –1.13, –1.33, –1.43, –1.55–3.19 Spin down: 2.16–3.31, 1.59, –0.30, –0.68, –1.32, –1.54–1.94, –2.15–2.56	Spin up: 1.42 Spin down: 1.89	1.32	1.10	1.57	1.35 (–0.35, 1.00)	–0.15, 1.20
3	$U = 4.0$: 2.96–3.50, 1.86–2.44, 0.22, –0.20, –0.43, –1.27, –1.55–2.50 GGA-PBE: –0.13, 0.19	0.42 0.32	0.58	0.24	1.26	0.67 (0.13, 0.80)	0.33, 1.00

^a The Fermi levels are set to zero. ^b Based on UV-Vis reflectance spectra. ^c Data are obtained using the Tris-HCl-buffered saline electrolyte.

Band structures of MOFs 1–3

In an attempt to further investigate the band structures of MOFs 1–3, spin-polarized DFT theoretical calculations were carried out using VASP software as described in the Experimental section. MOFs 1–3 were found to be paramagnetic, ferromagnetic and antiferromagnetic, respectively (Table S5†). Since Co^{2+} , Cu^{2+} and Ni^{2+} contain partially filled d orbitals, this could result in strongly correlated electron materials (SCEMs). We therefore used both the GGA-PBE method and GGA-PBE+U formalism as implemented in VASP following Dudarev's method⁵⁷ to calculate the band structures of MOFs 1–3.

The different U values ($U = 3.3$,^{58,79} 4.0; $U = 4.0$, $J = 1.0$;⁵⁹ $U = 5.0$, $J = 1.0$) have nearly no effect on the band structure and band gap of the paramagnetic MOF 1 (Table S6†). However, the plus U method was found less accurate than the simple GGA-PBE method for the E_g calculation of MOF 1 (Table S6† and Table 2). The band gap calculated using $U = 4.0$, $J = 1.0$, is 1.73 eV, while the GGA-PBE method gives 1.29 eV, perfectly consistent with the 1.28 eV found by the EC method. Tilset *et al.*⁸⁰ calculated the bandgap of the paramagnetic MOF-5 ($\text{Zn}_4\text{O}(\text{BDC})$ (BDC = 1,4-benzenedicarboxylate)) using the GGA-PBE method. The calculated result (3.5 eV) is in excellent agreement with the experimental value of 3.4–3.5 eV. Using the same method, the calculated band gap of a paramagnetic Sr-MOF, $[\text{Sr}(\text{HBTC})(\text{H}_2\text{O})]_n$ (H_3BTC = 1,2,4-benzenetricarboxylic

acid) is 2.04 eV,⁸¹ close to the experimental value (2.17 eV) obtained by the plot of $F(R)$ versus $h\nu$. These results suggest that the GGA-PBE method can accurately calculate the band gap of a paramagnetic material even if the metal ions containing unpaired electrons. The calculated band structure of MOF 1 by the GGA-PBE method is given in Fig. 7(a). As shown in Fig. 7(a), the top of the VB and the bottom of the CB of MOF 1 are flat and with very small dispersion (0.040 and 0.080 eV, respectively). As shown in Fig. S15,† the lowest energy of the CB and the VB maximum for MOF 1 are located at different points (G and X, respectively), indicating that MOF 1 has an indirect band gap. The calculated E_g according to the method for an indirect band gap semiconductor based on UV-Vis reflectance spectra was found to be 1.23 eV, consistent with the calculated values.

Similar to the calculations of MOF 1, the different U values ($U = 3.0$, 3.3, 4.0,^{58,79} 5.0; $U = 4.0$, $J = 1.0$ (ref. 59)) have nearly no effect on the band structure and the band gap of the antiferromagnetic MOF 3 (Table S6†). The band gaps are in the range of 0.39–0.40 eV, which is slightly more accurate than the value (0.32 eV) calculated by the GGA-PBE method (Table 2). The calculated band structure of 3 by the GGA-PBE+U ($U = 4.0$) method is given in Fig. 7(b). As shown in Fig. 7(b), the top of the VB and the bottom of the CB of MOF 3 are very flat and with very small dispersion (0.0030 and 0.0035 eV, respectively). As shown in Fig. S17,† the lowest energy of the CB and the VB maximum for MOF 3 are located at different points (X and G, respectively).

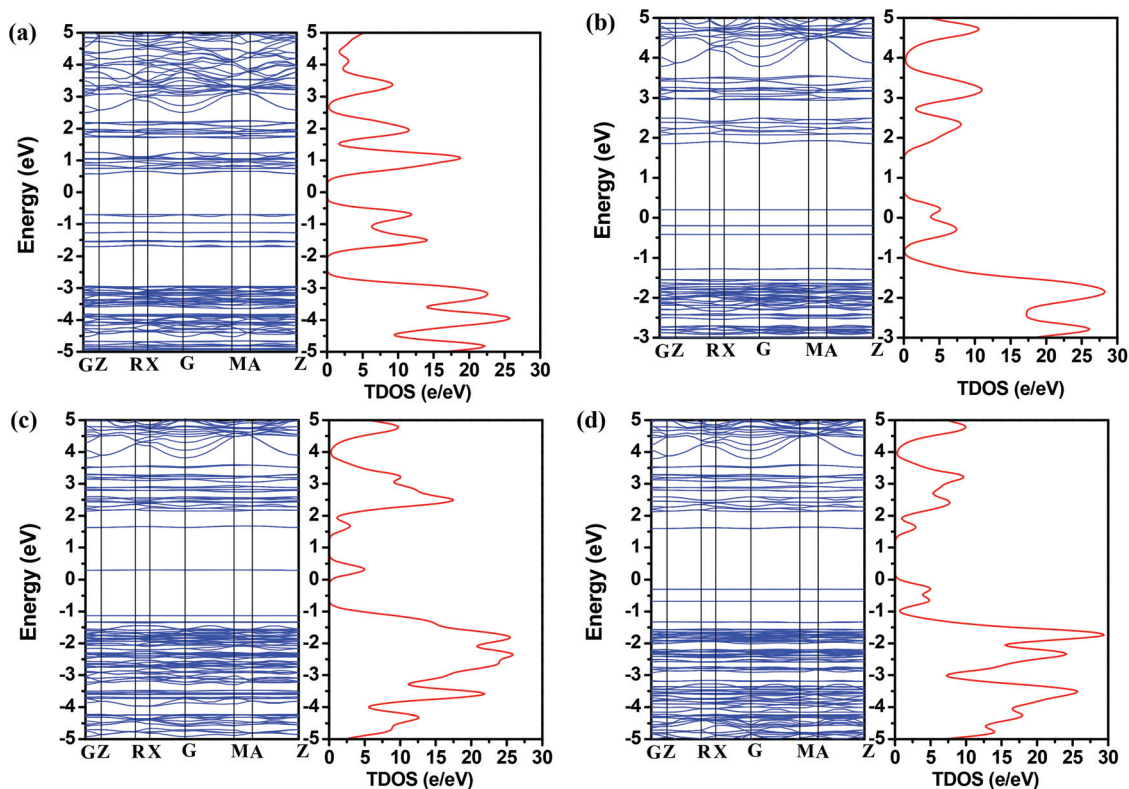


Fig. 7 Band structures and TDOS of MOFs 1 (a, PBE), 3 (b, $U = 4.0$) and 2 (spin-up: c, spin-down: d, $U = 3.3$). The Fermi levels are set to zero.

respectively), indicating that MOF 3 has an indirect band gap. The calculated E_g according to the method for an indirect band gap semiconductor based on UV-Vis reflectance spectra was found to be 0.24 eV, consistent with the calculated results (0.39–0.40 eV), however less accurate than the value (0.58 eV) calculated by the plot of $F(R)$ versus energy ($h\nu$) which is very similar to the E_g determined by the EC method (0.67 eV).

Different from the calculations of MOFs 1 and 3, the different U values ($U = 3.0, 3.3, 4.0, 6.4$ (ref. 58 and 79)) have a large effect on the band structure and band gap of the ferromagnetic MOF 2 (Table S7†). It was found that the calculated band gap 1.42 eV ($V_{\max} = -1.130$, $C_{\min} = 0.292$) of the spin-up electrons of 2 calculated using GGA-PBE ($U = 3.3$) is very close to the experimental result (1.35 eV), while the value of the spin down electrons is 1.89 eV ($V_{\max} = -0.300$, $C_{\min} = 1.594$), much larger than the experimental value (1.35 eV). The band gap considering all the electrons of MOF 2 is $0.292 - (-0.300) = 0.59$ eV. The experimental values fit with the band gap of the spin-up electrons, which might be due to the reason that the states of spin-up electrons are the majority states. The calculated band structure of 2 by the GGA-PBE+ U ($U = 3.3$) method is given in Fig. 7(c) and (d). As shown in Fig. 7(c), the top of the VB and the bottom of the CB of MOF 2 are very flat and with very small dispersion (the spin-up electrons: 0.0040 and 0.0015 eV, respectively; the spin down electrons: 0.0030 and 0.0047 eV, respectively). As shown in Fig. S16,† the lowest energy of the CB and the VB maximum for the spin-up and spin-down electrons of MOF 2 are located at different points (G and X, respectively), indicating that MOF 2 has an indirect band gap. The calculated E_g according to the method for an

indirect band gap semiconductor based on UV-Vis reflectance spectra was found to be 1.10 eV, consistent with the calculated results (1.42 eV), however less accurate than the value (1.32 eV) calculated by the plot of $F(R)$ versus energy ($h\nu$) which is very similar to the E_g determined by the EC method (1.35 eV). Thus, when the top of the VB and bottom of the CB are very flat like in the cases of MOFs 2 and 3, the experimental values of E_g determined by the plots of $F(R)$ versus energy ($h\nu$) seem to be the most accurate value compared to the value determined by the plots of $[F(R)h\nu]^{1/2}$ versus energy ($h\nu$) or the plots of $[F(R)h\nu]^2$ versus energy ($h\nu$) as shown in Table 2. The band structure of MOF [Sr(HBTC)(H₂O)]_n was found to be very flat, however showing that it has an indirect bandgap.⁸¹ Its calculated band gap is 2.04 eV, which fits better with the E_g determined using the plot of $F(R)$ versus $h\nu$ (2.17 eV) than with the E_g determined using the plot of $[F(R) \cdot h\nu]^{1/2}$ versus $h\nu$ (1.83 eV). Thus, we propose that when the top of the VB and bottom of the CB of a material are very flat (<0.005 eV), the experimental value for E_g should be determined using the plots of $F(R)$ versus energy ($h\nu$).

Since the calculated band gaps of MOFs 1–3 are close to the experimental values, we assume that the band structures of MOFs 1–3 were also determined correctly by the calculations. Based on the calculated band structures and the experimentally determined conduction and valence band-edge positions, the energy levels of MOFs 1–3 relative to the Ag/AgCl electrode (saturated KCl solution) and NHE (standard hydrogen electrode) were deduced and are given in Fig. 8. The band structures of MOFs 1–3 (shown in Fig. 7 and 8) are not continuous. They can all be regarded as semiconductors having

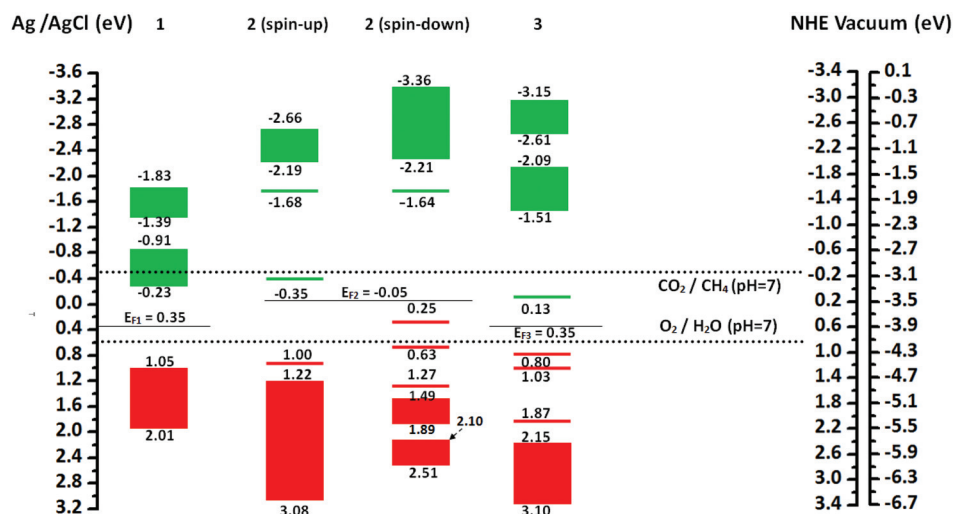


Fig. 8 Schematic energy level diagrams of MOFs 1–3 in comparison with the potentials for water oxidation to O₂ and CO₂ reduction to CH₄ in the presence of H₂O. Valence bands are in red, and conduction bands in green. The energy levels were determined based on experimental and calculated results. Numbers shown are vs. Ag/AgCl electrode. The valence and conduction band edge positions of MOF 1, spin-up electrons of 2, and 3 are determined by EC experiments; the valence and conduction band edge positions of the spin-down electrons of 2 are determined based on the calculated results and the experimental value of the conduction band edge of the spin-up electrons (−0.35 eV); and the rest positions are based on the calculated band structures. E_{F1} , E_{F2} , E_{F3} are the Fermi levels of MOFs 1–3 vs. the Ag/AgCl electrode, determined based on the calculated band structures and experimental values of the conduction band edge positions.

intermediate bands (IB) (MOF 1) or levels (MOF 2 and 3). The use of intermediate bands (IB) or levels lying within the band gap of a semiconductor has been proposed as a means of manufacturing solar cells with efficiencies of up to 63.3% under ideal conditions.⁸² IB materials can not only utilize the photons which could pump electrons from the VB to the CB as the cases for traditional semiconductors, but also utilize photons which could pump electrons from the VB to the IB or from the IB to the CB.⁸³ For example, due to the existence of the IB (−0.23–0.91 eV) in MOF 1, electrons can be excited from the VB at 1.05–2.01 eV to the IB, from the IB to the CB at −1.39–−1.83 eV and from the VB to the CB at −1.39–−1.83 eV (Fig. 8), thus increasing the visible light utilization efficiencies. MOFs 1–3 are bulk IB materials without impurity doping, which reduces densities and therefore lowers absorption levels when utilized in solar cells.⁸⁴

The positions of the valence and conduction band edges or levels of MOFs 1–3 relative to the potential of the reduction of CO₂ (in the presence of H₂O) to CH₄ (eqn (1)) and the oxidation of H₂O to O₂ (eqn (2)) (Fig. 8) suggest that the photo-generated electrons and holes in MOFs 1–3 can reduce CO₂ to CH₄, and at the same time oxidize H₂O into O₂ under visible light. For example, MOF 3 can absorb visible light with 2.31–3.0 eV energy and cause electrons in the orbitals at 0.80 or 1.03 eV to the conduction band at −1.51–−2.09 eV (Fig. 8). The excited electrons can reduce CO₂ to CH₄, and the holes left in the orbitals at 0.80 eV can oxidize H₂O into O₂ as shown in Fig. 13. The Fermi levels of MOFs 2–3 are close to their intermediate levels, suggesting that these states might be partially filled with electrons at room temperature. In contrast, the Fermi level of MOF 1 is relatively far away from the band edges of the IB and VB (Fig. 8).

Mid-gap levels in semiconductors have been well known for a long time. They can act as very effective recombination centres, thus jeopardizing the potential of IB solar cells.^{85–89} However, Antolín *et al.* found that when the densities of these levels are sufficiently high, it will suppress the non-radiative recombination and thus can increase the solar cell efficiency.⁸²

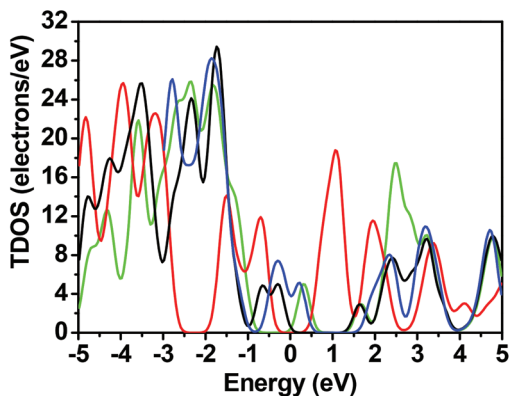
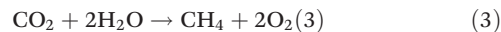
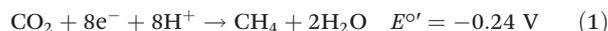


Fig. 9 The comparison of the TDOS of MOF 1 (spin-up electrons, red line), 2 (spin-up electrons: green; spin-down electrons: black) and 3 (spin-up electrons, blue).

Fig. 7 and 8 show that the band structure of MOF 1 has an extended IB, but MOFs 2 and 3 have discrete intermediate levels. In addition, the density of states of the VB, IB and CB bands of MOF 1 are much higher than those of MOF 2 and MOF 3 (Fig. 9). The band structures of MOFs 1–3 also reveal that the thermodynamic driving force for H₂O oxidation is greater for MOF 1 than for MOFs 2–3 since its valence band edges are much lower with respect to the water oxidation level than the cases for MOFs 2–3.⁹⁰ The above results suggest that the photocatalytic activity of MOF 1 should be significantly better than those of MOFs 2 and 3. Consistently, experimental results (see below) did find that MOFs 2 and 3 have low photocatalytic activity and MOF 1 has high photocatalytic activity for CO₂ reduction to methane.



(E° is the reduction potential in pH = 7.0 aqueous solution).

Orbital populations of MOFs 1–3

The total and partial density of states (DOS) of MOFs 1–3 are shown in Fig. 9 and 10. Since the DOS patterns of the spin-up electrons are identical to those of the spin-down electrons for MOFs 1 and 3, only the DOS patterns of the spin-up electrons of MOFs 1 and 3 are given. The top of the VB in MOF 1 is mainly composed of Co 3d states, and the bottom of the CB in MOF 1 is dominated by C 2p, N 2p, O 2p and Co 3d states as shown in Fig. 10(a). As shown in Fig. 10(b), the top of the VB of the spin-up and spin down electrons in MOF 2 is mainly composed of Ni 3d states and some O 2p states, and the bottom of the CB of the spin-up and spin-down electrons of 2 is dominated by Ni 3d states and some N 2p states. As shown in Fig. 10(c), the top of the VB in MOF 3 is mainly composed of Cu 3d states, and some N 2p and O 2p states, and the bottom of the CB in MOF 3 is dominated by Cu 3d states and some O 2p states. Thus, the 3d states of Cu(II), Co(II) and Ni(II) contribute significantly to the valence band and conduction band edges of MOF structures.

Photoelectric properties of MOFs 1–3

Photovoltaic applications of MOFs belong to a relatively new area of research and there have been only a few reports on the optoelectronic properties of MOFs.^{8–13,91,92}

The photoelectrical properties of MOFs 1–3 were studied in a three-electrode set-up. Fig. 11 shows the rapid photocurrent responses of MOFs 1–3 for each switch-on and switch-off event under UV and visible light illumination and the signals are stable. MOFs 1–3 exhibit anodic photocurrent, and the photocurrent increases with increasing anodic potential, suggesting a quick recombination of photogenerated electrons and holes under a lower potential bias. Under the same conditions, we found that the photocurrent intensities generated using 430 nm light increase in the order of MOF 3 < 1 < 2, respect-

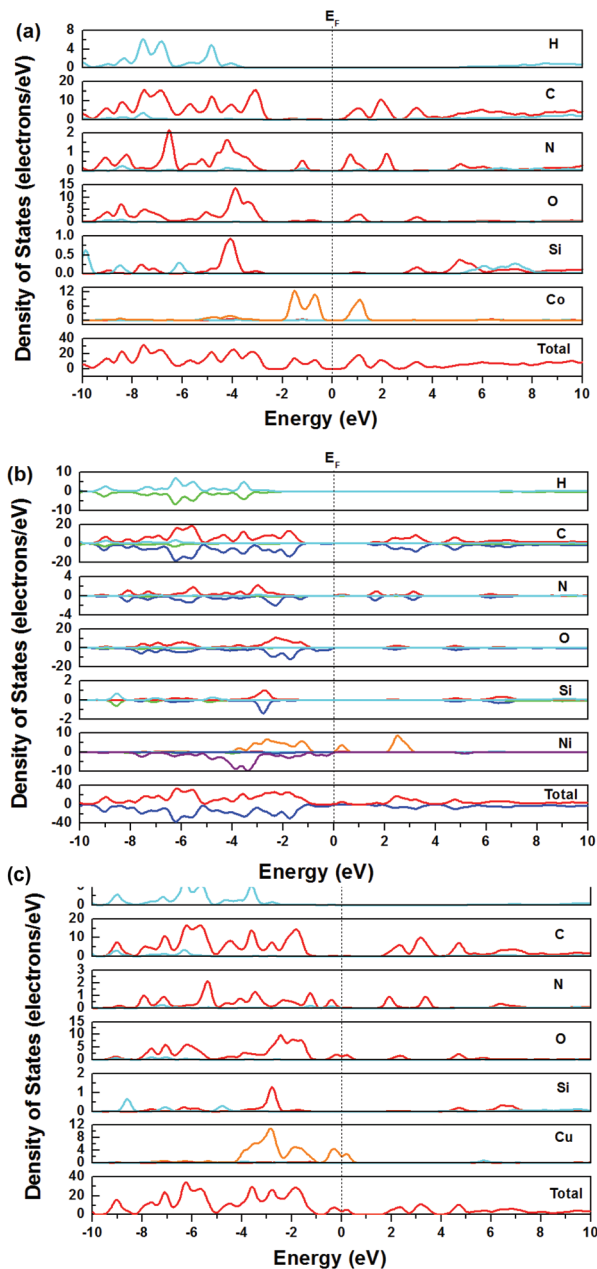


Fig. 10 TDOS and PDOS of MOFs 1 (a) and 2 (b) and 3 (c). In the PDOS, cyan, red, and orange lines represent spin-up s, p and d orbitals, respectively; and green, blue and magenta lines represent spin-down s, p and d orbitals, respectively. The Fermi levels are set to zero.

ively. Although MOFs 1–3 absorb widely in the UV and visible light region, it is found that the photocurrent densities in the visible light region are lower than those values under UV light for all the three MOFs, suggesting the faster recombination of the photogenerated electrons and holes under visible light illumination.¹¹

Photocatalytic reduction of CO₂ to methane

Consistent with theoretical predictions, all of the three MOFs were found to be able to catalyze the reduction of CO₂ to CH₄

under xenon light, the spectrum of which is very similar to sun light. The catalytic activities of MOF 1 (0.75 $\mu\text{mol g}^{-1}$ after 4 h) are significantly better than those of MOFs 2 and 3 (0.14 $\mu\text{mol g}^{-1}$ after 4 h) (Fig. 12). The catalytic activity of MOFs 1 and 3 under visible light was further checked. The photocatalytic CH₄ evolution amounts using MOF 1 increase to 1.44 $\mu\text{mol g}^{-1}$ after 8 h, which is higher than the 0.95 $\mu\text{mol g}^{-1}$ obtained under the whole spectrum light of the Xe lamp due to its higher activation temperature (150 *versus* 60 °C). The higher activation temperature can make the sample absorb more CO₂ in the experiment, leading to higher catalytic activity. The above observation also suggests that UV light contributes little to the catalytic process. The catalytic activity of MOF 1 decreases when the samples were heated at a lower temperature (120 °C).

The mechanism was proposed as shown in Fig. 13. The photogenerated electrons and holes in the illuminated MOFs 1–3 reacted with the adsorbed CO₂ and H₂O to produce CH₄ and O₂ according to eqn (1)–(2), giving the overall reaction as shown in eqn (3). Due to the test limitation of our GC instru-

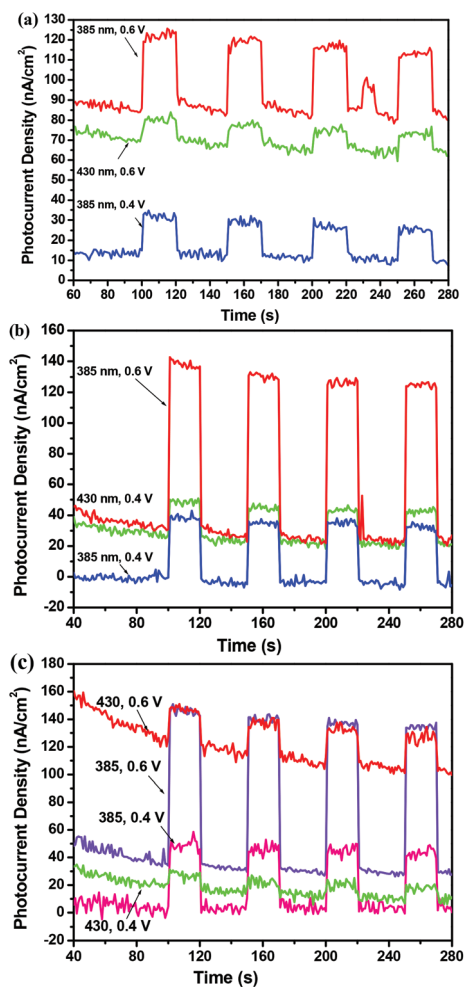


Fig. 11 MOF 1 (a), 2 (b) and 3 (c) irradiated with 385 or 430 nm light at 0.4 and 0.6 V.

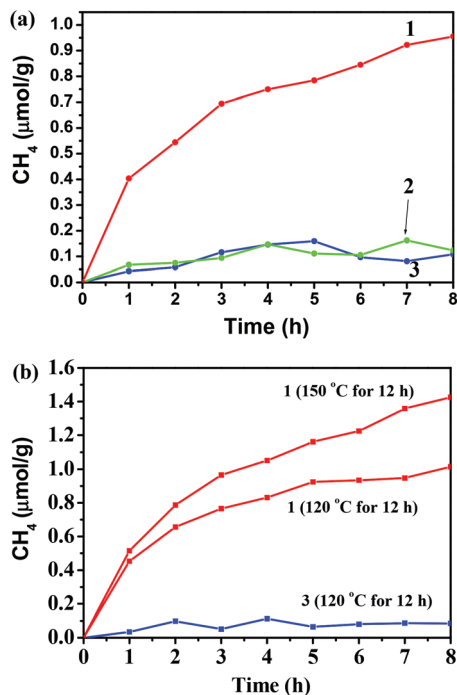


Fig. 12 Photocatalytic CH₄ evolution amounts for MOFs 1–3 as a function of light irradiation time with a Xe lamp. (a) Without filter. MOFs 1–3 were heated in a 60 °C oven for 12 h before carrying out the photocatalytic experiments. (b) Under visible light (wavelength: ≥ 420 nm). Samples were heated in a 120 °C or 150 °C oven for 12 h before carrying out the photocatalytic experiment.

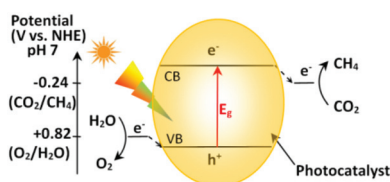


Fig. 13 Proposed mechanism for the photocatalytic reduction of CO₂ by water.

ment, we only detected CH₄ in our experiments. The photocatalytic efficiency of MOF 1 is much better than that of our previously reported pure Na₂V₆O₁₆·xH₂O nanoribbons (0.07 $\mu\text{mol g}^{-1}$ after 8 h) and similar to the 1 wt% RuO₂ and 1 wt% Pt coloaded Na₂V₆O₁₆·xH₂O nanoribbons (1.51 $\mu\text{mol g}^{-1}$ after 8 h), the results of which are obtained under the same experimental conditions as those of MOF 1.⁹³ The higher activity of MOF 1 could be due to its CO₂ storage capability, making CO₂ readily available to react with the electrons produced during the illumination under light. Li *et al.* also reported that the high storage capability of CO₂ can increase the efficiency of photocatalysts.¹⁴

The photocatalytic reactions were carried out at 298 K and 1 atm. The diameters of the channels of MOFs 1–3 are not more than 1.6×3.6 Å (Table S4†, *a + b* direction). The kinetic dia-

eters of N₂, CH₄, CO₂ and H₂O are 3.64, 3.80, 3.30 and 2.65 Å respectively.⁹⁴ Consistently the isotherms of the adsorption of N₂ and CH₄ of MOFs 1–3 at 298 K are nearly linear, indicating that the adsorption of these molecules occurred on the surfaces of the materials, not in the pores. The isotherms of the adsorption of CO₂ of MOFs 1–3 at 298 K are not completely linear, indicating that a small portion of CO₂ adsorption occurred in the channels. The CO₂ in the channels would not be significant due to the small diameters of the channels and the low porosities of MOFs 1–3 (Table S4†). Thus we deduce that the majority of the photocatalytic reactions occurred on the surfaces of MOFs 1–3. The small amounts of CO₂ in the pores could receive 8e⁻ and 8H⁺ to form CH₄ and 2H₂O. However, the formed CH₄ in the pore would have difficulty in coming out of the pores due to the small diameters of the channels.

Probably because of the involvement of the transfer of 8 electrons, the photocatalytic reduction of CO₂ to CH₄ using MOFs has seldom been reported.^{14,15} Li *et al.* reported that a MOF CPO-27-Mg/TiO₂ nanocomposite shows no CO₂ reduction properties under visible light, but produced 40.9 $\mu\text{mol g}^{-1}$ of CO and 23.5 $\mu\text{mol g}^{-1}$ of CH₄ after 10 h irradiation with 365 nm UV light.¹⁴ Strunk and Fischer *et al.* reported that NH₂-MIL-125 (a Ti-containing MOF) derived TiO₂/GNPs (gold nanoparticles) produced 61 ppm CH₄ (0.0024–0.0032 $\mu\text{mol g}^{-1} \text{ h}^{-1}$) after 6 h illumination with a 200 W Hg/Xe (250–750 nm) lamp.¹⁵ The unusual photochemical properties of MOFs 1–3 can be related to their band structures. The calculations show that all the three MOFs can be viewed as bulk IB materials. MOF 1 is a better photocatalyst than MOFs 2 and 3 since the density of states of the IB in MOF 1 is high, which could suppress the non-radioactive recombination.⁸² The density of states of the IB levels in MOFs 2 and 3 are low, making these levels very effective recombination centres, thus jeopardizing the photocatalytic activities of MOFs 2 and 3.^{85–89}

Conclusions

Three water-stable isostructural, two-fold interpenetrated paddlewheel MOFs of [M₂(TCS)(BPY)] [M = Co(1) and Ni(2) and Cu(3)] were synthesized and characterized. MOFs 1–3 are stable in pH = 5–11, 2–11, 3–11 aqueous solution, respectively. They are stable after heating at 150–200 °C for at least 12 h, which are sufficient to remove the trapped solvent molecules. Their gas storage properties for H₂, CO₂ and CH₄ have been studied, showing good H₂, moderate CO₂ and CH₄ storage capacity. MOFs 1–3 absorb visible light in broad ranges with the band gaps of 1.28, 1.35 and 0.67 eV, respectively. The photocurrent densities generated by these MOFs upon visible light (430 nm) illumination increase in the order of MOF 3 < 1 < 2.

All the three MOFs exhibit rare photocatalytic activities toward CO₂ reduction to CH₄ under visible light, producing 0.75 $\mu\text{mol g}^{-1}$ (MOF 1) and 0.14 $\mu\text{mol g}^{-1}$ (MOFs 2 and 3) under xenon light after 4 h, respectively. Calculations suggest that the better photocatalytic properties of MOF 1 than those

of MOFs 2 and 3 are likely due to the higher density of states of the intermediate band in MOF 1. Our results show that the photo-physical and chemical properties of MOFs can be tuned by using electron-rich metal ions. This work demonstrates for the first time that calculations can be successfully applied to address the question of how the types of unpaired electron containing electron-rich metal ions (*i.e.* Cu(II), Co(II), Ni(II)) affect the band gaps and band structures of MOFs. More semiconducting MOFs with excellent photo-physical and chemical properties could be designed and prepared by using this approach.

Acknowledgements

We thank the National Natural Science Foundation of China (NSFC) (no. 21071082, 21403115), the Natural Science Foundation of Jiangsu Province (no. BK20150045), and the Natural Science Foundation of Education Department of Jiangsu Province (no. 16KJB150021) for their funding support.

Notes and references

- W. G. Tu, Y. Zhou and Z. G. Zou, *Adv. Mater.*, 2014, **26**, 4607–4626.
- N. Armaroli and V. Balzani, *Chem. – Eur. J.*, 2016, **22**, 32–57.
- D. Chen, X. G. Zhang and A. F. Lee, *J. Mater. Chem. A*, 2015, **3**, 14487–14516.
- C. G. Silva, A. Corma and H. Garcia, *J. Mater. Chem. A*, 2010, **20**, 3141–3156.
- M. Usman, S. Mendiratta and K.-L. Lu, *Adv. Mater.*, 2016, **28**, 1–5.
- J. Wang, J. Sun, C. Hu, Z. Liu and S. Hu, *J. Electroanal. Chem.*, 2015, **759**, 2–7.
- L. P. Zhang, P. Cui, H. B. Yang, J. Z. Chen, F. X. Xiao, Y. Y. Guo, Y. Liu, W. N. Zhang, F. W. Huo and B. Liu, *Adv. Sci.*, 2016, **3**, 1500243.
- D. Q. Jin, Q. Xu, L. Y. Yu and X. Y. Hu, *Microchim. Acta*, 2015, **182**, 1885–1892.
- J. I. Feldblyum, E. A. Keenan, A. J. Matzger and S. Maldonado, *J. Phys. Chem. C*, 2012, **116**, 3112–3121.
- Y. Horiuchi, T. Toyao, K. Miyahara, L. Zakary, V. Dang Do, Y. Kamata, T.-H. Kim, S. W. Lee and M. Matsuoka, *Chem. Commun.*, 2016, **52**, 5190–5193.
- Y. An, H. Li, Y. Liu, B. Huang, Q. Sun, Y. Dai, X. Qin and X. Zhang, *J. Solid State Chem.*, 2016, **233**, 194–198.
- P. G. Jiang, P. Zhang, Y. Gong and J. H. Lin, *Dalton Trans.*, 2016, **45**, 4603–4613.
- J. K. Gao, J. W. Miao, P. Z. Li, W. Y. Teng, L. Yang, Y. L. Zhao, B. Liu and Q. C. Zhang, *Chem. Commun.*, 2014, **50**, 3786–3788.
- M. T. Wang, D. K. Wang and Z. H. Li, *Appl. Catal., B*, 2016, **183**, 47–52.
- K. Khaletskaya, A. Pougin, R. Medishetty, C. Rosler, C. Wiktor, J. Strunk and R. A. Fischer, *Chem. Mater.*, 2015, **27**, 7248–7257.
- Z.-G. Gu, L. Heinke, C. Woell, T. Neumann, W. Wenzel, Q. Li, K. Fink, O. D. Gordan and D. R. T. Zahn, *Appl. Phys. Lett.*, 2015, **107**, 183301.
- A. Fateeva, P. A. Chater, C. P. Ireland, A. A. Tahir, Y. Z. Khimyak, P. V. Wiper, J. R. Darwent and M. J. Rosseinsky, *Angew. Chem., Int. Ed.*, 2012, **51**, 7440–7444.
- P. Lu, Y. Wu, H. Kang, H. Wei, H. Liu and M. Fang, *J. Mater. Chem. A*, 2014, **2**, 16250–16267.
- J. J. Wang, J. Zhang, F. Y. Jin, Y. P. Luo, S. F. Wang, Z. Y. Zhang, Y. Wu, H. K. Liu, J. Y. Luc and M. Fang, *CrystEngComm*, 2015, **17**, 5906–5910.
- S. F. Wang, J. J. Wang, W. W. Cheng, X. W. Yang, Z. Y. Zhang, Y. Xu, H. K. Liu, Y. Wu and M. Fang, *Dalton Trans.*, 2015, **44**, 8049–8061.
- N. ul Qadir, S. A. M. Said and H. M. Bahaidarah, *Microporous Mesoporous Mater.*, 2015, **201**, 61–90.
- P. W. Li, J. H. Chen, J. Y. Zhang and X. L. Wang, *Sep. Purif. Rev.*, 2015, **44**, 19–27.
- K. S. Park, Z. Ni, A. P. Cote, J. Y. Choi, R. Huang, F. J. Uribe-Romo, H. K. Chae, M. O’Keeffe and O. M. Yaghi, *Proc. Natl. Acad. Sci. U. S. A.*, 2006, **103**, 10186–10191.
- K. A. Cychosz and A. J. Matzger, *Langmuir*, 2010, **26**, 17198–17202.
- D. Y. Hong, Y. K. Hwang, C. Serre, G. Ferey and J. S. Chang, *Adv. Funct. Mater.*, 2009, **19**, 1537–1552.
- W. M. Bloch, R. Babarao, M. R. Hill, C. J. Doonan and C. J. Sumby, *J. Am. Chem. Soc.*, 2013, **135**, 10441–10448.
- E. Sanchez-Gonzalez, J. R. Alvarez, R. A. Peralta, A. Campos-Reales-Pineda, A. Tejada-Cruz, E. Lima, J. Balmaseda, E. Gonzalez-Zamora and I. A. Ibarra, *ACS Omega*, 2016, **1**, 305–310.
- J. R. Alvarez, R. A. Peralta, J. Balmaseda, E. Gonzalez-Zamora and I. A. Ibarra, *Inorg. Chem. Front.*, 2015, **2**, 1080–1084.
- R. A. Peralta, B. Alcantar-Vazquez, M. Sanchez-Serratos, E. Gonzalez-Zamora and I. A. Ibarra, *Inorg. Chem. Front.*, 2015, **2**, 898–903.
- J. Liu, F. Zhang, X. Q. Zou, G. L. Yu, N. Zhao, S. J. Fan and G. S. Zhu, *Chem. Commun.*, 2013, **49**, 7430–7432.
- J. H. Cavka, S. Jakobsen, U. Olsbye, N. Guillou, C. Lamberti, S. Bordiga and K. P. Lillerud, *J. Am. Chem. Soc.*, 2008, **130**, 13850–13851.
- I. M. Hauptvogel, R. Biedermann, N. Klein, I. Senkovska, A. Cadiau, D. Wallacher, R. Feyerherm and S. Kaskel, *Inorg. Chem.*, 2011, **50**, 8367–8374.
- Y. Ling, Z. Chen, H. Zheng, Y. Zhou, L. Weng and D. Zhao, *Cryst. Growth Des.*, 2011, **11**, 2811–2816.
- Z. J. Lin, T. F. Liu, X. L. Zhao, J. Lü and R. Cao, *Cryst. Growth Des.*, 2011, **11**, 4284–4287.
- K. Tan, N. Nijem, P. Canepa, Q. Gong, J. Li, T. Thonhauser and Y. J. Chabal, *Chem. Mater.*, 2012, **24**, 3153–3167.
- B. Zhang and Z. Wang, *Chem. Mater.*, 2010, **22**, 2780–2789.
- R. P. Davies, R. J. Less, P. D. Lickiss, K. Robertson and A. J. P. White, *Inorg. Chem.*, 2008, **47**, 9958–9964.

- 38 J. B. Lambert, Z. Q. Liu and C. Q. Liu, *Organometallics*, 2008, **27**, 1464–1469.
- 39 R. P. Davies, R. Less, P. D. Lickiss, K. Robertson and A. J. P. White, *Cryst. Growth Des.*, 2010, **10**, 4571–4581.
- 40 R. P. Davies, P. D. Lickiss, K. Robertson and A. J. P. White, *Aust. J. Chem.*, 2011, **64**, 1237–1244.
- 41 J. M. Gotthardt, K. F. White, B. F. Abrahams, C. Ritchie and C. Boskovic, *Cryst. Growth Des.*, 2012, **12**, 4425–4430.
- 42 M. W. Zhang, Y. P. Chen and H. C. Zhou, *CrystEngComm*, 2013, **15**, 9544–9552.
- 43 S. Mandic, M. R. Healey, J. M. Gotthardt, K. G. Alley, R. W. Gable, C. Ritchie and C. Boskovic, *Eur. J. Inorg. Chem.*, 2013, 1631–1634.
- 44 Y. S. Xue, L. Zhou, M. P. Liu, M. Liu, Y. Xu, H. B. Du and X. Z. You, *CrystEngComm*, 2013, **15**, 6229–6236.
- 45 Y. X. Li, M. Xue, L. J. Guo, L. Huang, S. R. Chen and S. L. Qiu, *Chem. Res. Chin. Univ.*, 2013, **29**, 196–200.
- 46 Y. X. Li, M. Xue, L. Huang, S. R. Chen and S. L. Qiu, *Chem. Res. Chin. Univ.*, 2013, **29**, 611–616.
- 47 D. W. Feng, K. C. Wang, Z. W. Wei, Y. P. Chen, C. M. Simon, R. K. Arvapally, R. L. Martin, M. Bosch, T. F. Liu, S. Fordham, D. Q. Yuan, M. A. Omary, M. Haranczyk, B. Smit and H. C. Zhou, *Nat. Commun.*, 2014, **5**, 5723.
- 48 Y. X. Li, M. Xue, L. J. Guo, L. Huang, S. R. Chen and S. L. Qiu, *Inorg. Chem. Commun.*, 2013, **28**, 25–30.
- 49 M. W. Zhang, M. Bosch and H. C. Zhou, *CrystEngComm*, 2015, **17**, 996–1000.
- 50 J. H. Lee, B. Moon, T. K. Kim, S. Jeoung and H. R. Moon, *Dalton Trans.*, 2015, **44**, 15130–15134.
- 51 G. Kresse and D. Joubert, *Phys. Rev. B: Condens. Matter*, 1999, **59**, 1758–1775.
- 52 P. E. Blochl, *Phys. Rev. B: Condens. Matter*, 1994, **50**, 17953–17979.
- 53 J. P. Perdew, K. Burke and Y. Wang, *Phys. Rev. B: Condens. Matter*, 1996, **54**, 16533–16539.
- 54 J. P. Perdew, K. Burke and M. Ernzerhof, *Phys. Rev. Lett.*, 1996, **77**, 3865–3868.
- 55 J. P. Perdew, *Electron Structure of Solids*, Akademie Verlag, Berlin, 1991.
- 56 N. J. Mosey, P. Liao and E. A. Carter, *J. Chem. Phys.*, 2008, **129**, 014103.
- 57 S. L. Dudarev, G. A. Botton, S. Y. Savrasov, C. J. Humphreys and A. P. Sutton, *Phys. Rev. B: Condens. Matter*, 1998, **57**, 1505–1509.
- 58 L. Wang, T. Maxisch and G. Ceder, *Phys. Rev. B: Condens. Matter*, 2006, **73**, 195107.
- 59 J. Zhou and Q. Sun, *J. Am. Chem. Soc.*, 2011, **133**, 15113–15119.
- 60 Q. Zhang, B. Li and L. Chen, *Inorg. Chem.*, 2013, **52**, 9356–9362.
- 61 Q. X. Yao, J. L. Sun, K. Li, J. Su, M. V. Peskov and X. D. Zou, *Dalton Trans.*, 2012, **41**, 3953–3955.
- 62 N. Klein, I. Senkovska, I. A. Baburin, R. Gruenker, U. Stoeck, M. Schlichtenmayer, B. Streppel, U. Mueller, S. Leoni, M. Hirscher and S. Kaskel, *Chem. – Eur. J.*, 2011, **17**, 13007–13016.
- 63 J. B. DeCoste, G. W. Peterson, B. J. Schindler, K. L. Killups, M. A. Browe and J. J. Mahle, *J. Mater. Chem. A*, 2013, **1**, 11922–11932.
- 64 J. B. DeCoste, G. W. Peterson, H. Jasuja, T. G. Glover, Y. G. Huang and K. S. Walton, *J. Mater. Chem. A*, 2013, **1**, 5642–5650.
- 65 M. P. Suh, H. J. Park, T. K. Prasad and D. W. Lim, *Chem. Rev.*, 2012, **112**, 782–835.
- 66 Y. He, W. Zhou, G. Qian and B. Chen, *Chem. Soc. Rev.*, 2014, **43**, 5657–5678.
- 67 K. Sumida, D. L. Rogow, J. A. Mason, T. M. McDonald, E. D. Bloch, Z. R. Herm, T. H. Bae and J. R. Long, *Chem. Rev.*, 2012, **112**, 724–781.
- 68 C. R. Wade and M. Dincă, *Dalton Trans.*, 2012, **41**, 7931–7938.
- 69 S. R. Caskey, A. G. Wong-Foy and A. J. Matzger, *J. Am. Chem. Soc.*, 2008, **130**, 10870–10871.
- 70 W. Zhou, H. Wu and T. Yildirim, *J. Am. Chem. Soc.*, 2008, **130**, 15268–15269.
- 71 J. Guo, J. F. Ma, B. Liu, W. Q. Kan and J. Yang, *Cryst. Growth Des.*, 2011, **11**, 3609–3621.
- 72 L. Liu, J. Ding, M. Li, X. Lv, J. Wu, H. Hou and Y. Fan, *Dalton Trans.*, 2014, **43**, 12790–12799.
- 73 M. A. Butler, *J. Appl. Phys.*, 1977, **48**, 1914–1920.
- 74 G. Q. Zhang, W. Wang, Q. X. Yu and X. G. Li, *Chem. Mater.*, 2009, **21**, 969–974.
- 75 Z. Sha and J. Wu, *RSC Adv.*, 2015, **5**, 39592–39600.
- 76 A. E. Morales, E. S. Mora and U. Pal, *Rev. Mex. Fis. S*, 2007, **53**, 18–22.
- 77 T.-F. Yeh, S.-J. Chen, C.-S. Yeh and H. Teng, *J. Phys. Chem. C*, 2013, **117**, 6516–6524.
- 78 G.-L. Wang, J.-X. Shu, Y.-M. Dong, X.-M. Wu, W.-W. Zhao, J.-J. Xu and H.-Y. Chen, *Anal. Chem.*, 2015, **87**, 2892–2900.
- 79 K. Lee, J. D. Howe, L.-C. Lin, B. Smit and J. B. Neaton, *Chem. Mater.*, 2015, **27**, 668–678.
- 80 L.-M. Yang, P. Vajeeston, P. Ravindran, H. Fjellvag and M. Tilset, *Inorg. Chem.*, 2010, **49**, 10283–10290.
- 81 M. Usman, S. Mendiratta, S. Batjargal, G. Haider, M. Hayashi, N. R. Gade, J. W. Chen, Y. F. Chen and K. L. Lu, *ACS Appl. Mater. Interfaces*, 2015, **7**, 22767–22774.
- 82 A. Luque, A. Martí, E. Antolín and C. Tablero, *Physica B*, 2006, **382**, 320–327.
- 83 A. Marti, E. Antolin, C. R. Stanley, C. D. Farmer, N. Lopez, P. Diaz, E. Canovas, P. G. Linares and A. Luque, *Phys. Rev. Lett.*, 2006, **97**, 247701.
- 84 A. Luque, A. Marti and C. Stanley, *Nat. Photonics*, 2012, **6**, 146–152.
- 85 J. Wang, D. N. Tafen, J. P. Lewis, Z. Hong, A. Manivannan, M. Zhi, M. Li and N. Wu, *J. Am. Chem. Soc.*, 2009, **131**, 12290–12297.
- 86 W. Y. Choi, A. Termin and M. R. Hoffmann, *J. Phys. Chem.*, 1994, **98**, 13669–13679.
- 87 T. Miyagi, M. Kamei, I. Sakaguchi, T. Mitsuhashi and A. Yamazaki, *Jpn. J. Appl. Phys., Part 1*, 2004, **43**, 775–776.

- 88 D. N. Tafen, J. Wang, N. Wu and J. P. Lewis, *Appl. Phys. Lett.*, 2009, **94**, 093101.
- 89 M. A. Henderson, J. M. White, H. Uetsuka and H. Onishi, *J. Am. Chem. Soc.*, 2003, **125**, 14974–14975.
- 90 J. Li and N. Wu, *Catal. Sci. Technol.*, 2015, **5**, 1360–1384.
- 91 P. Zhang, Y. Gong and J. H. Lin, *Eur. J. Inorg. Chem.*, 2016, 322–329.
- 92 G. Z. Wang, Q. L. Sun, Y. Y. Liu, B. B. Huang, Y. Dai, X. Y. Zhang and X. Y. Qin, *Chem. – Eur. J.*, 2015, **21**, 2364–2367.
- 93 S. C. Feng, X. Y. Chen, Y. Zhou, W. G. Tu, P. Li, H. J. Li and Z. G. Zou, *Nanoscale*, 2014, **6**, 1896–1900.
- 94 A. F. Ismail, K. Khulbe and T. Matsuura, *Gas Separation Membranes: Polymeric and Inorganic*, Springer, 2015.